ACS Catalysis

Research Article

pubs.acs.org/acscatalysis

Role of Site Stability in Methane Activation on $Pd_xCe_{1-x}O_\delta$ Surfaces

Thomas P. Senftle,[†] Adri C. T. van Duin,[‡] and Michael J. Janik*,[†]

[†]Department of Chemical Engineering and [‡]Department of Mechanical and Nuclear Engineering, Pennsylvania State University, University Park, Pennsylvania 16802, United States

Supporting Information

ABSTRACT: Doped metal oxide catalysts can be optimized by identifying dopant metal/host oxide combinations that exhibit synergistic interactions not present in the parent systems. This is exemplified by $Pd_xCe_{1-x}O_\delta$ mixed oxides that yield methane oxidation rates unobtainable by the separate systems. Here we demonstrate that rapid C−H activation on $Pd_xCe_{1-x}O_\delta$ catalysts can be attributed to emergent behavior of the doped oxide enabling $Pd^{4+} \leftrightarrow Pd^{2+}$ transitions not evident in catalysts featuring a PdO_x active phase. $Pd_xCe_{1-x}O_\delta$ surfaces activate methane through hydrogen abstraction over Pd^{4+} surface states, in contrast to the σ-complex activation route favored over PdO_x surfaces. The stability of the active Pd^{4+} state is dependent on temperature and oxygen pressure during catalytic operation, and as such we combine reaction kinetics and thermodynamic stability arguments from density functional theory (DFT) calculations to derive the apparent methane activation barrier. This accounts for varying conditions affecting the stability of the Pd^{4+} state, demonstrating that active Pd^{4+} sites are metastable. These states form under the reaction environment and offer lower methane activation barriers in comparison to Pd^{2+} states. The Pd^{4+} state is stabilized by the incorporation of Pd in the fluorite lattice structure of CeO_2, which in turn provides unique methane activation chemistry from the $Pd_xCe_{x-1}O_\delta$ mixture. We generalize these results over (T,P) space by deriving phase boundaries demarcating regions where each Pd surface oxidation state is thermodynamically stable or kinetically active. The approach presented here can be readily extended to other systems, providing a method for assessing the interplay between site activity and stability on catalytic surfaces.

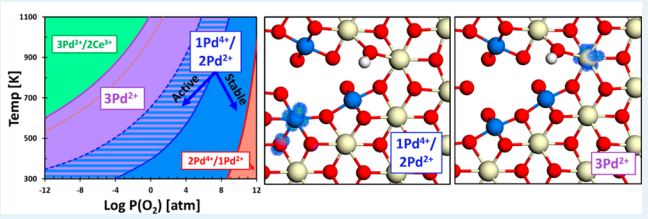

KEYWORDS: *ceria, palladium, methane oxidation, DFT, ab initio thermodynamics*

1. INTRODUCTION

Catalysts featuring mixed-metal oxides offer unique opportunities to tune the catalytic properties of a system by selecting metal/oxide combinations tailored to the target reaction process.[1] In such catalysts, dopant transition-metal ions are substituted into the lattice structure of a host oxide, resulting in a system with surface chemistry vastly different from that of the parent systems. Activity, selectivity, and stability may be tuned by searching for metal dopant/host oxide combinations that display desired catalytic properties. Hence, understanding the interaction between the metal dopant and the host oxide under reaction conditions is paramount to improving the design of a particular catalyst.

Doped oxides are of particular interest for catalytic combustion applications seeking efficient and clean utilization of hydrocarbon feedstocks.[2−6] Methane is readily available from natural gas deposits, and as such there is growing interest in catalysts that can activate methane at low temperatures.[6−10] Catalytic systems featuring Pd supported on CeO_2 demonstrate exceptional activity toward hydrocarbon oxidation, which can be attributed to synergistic Pd−ceria interactions.[5,6,8,9,11−17] The Pd−ceria system exemplifies mixed metal oxide catalysis that is enhanced by chemical properties not available in the parent systems. In this work we use density functional theory (DFT) in conjunction with ab initio thermodynamics to investigate methane activation kinetics and site stability on Pd-doped CeO_2 surfaces. This approach can be readily extended to other doped metal oxide systems, allowing one to identify and exploit emergent catalytic chemistry between metal dopants and oxide supports.

Depending on the catalyst preparation, pretreatment, and reaction environment, Pd can exist on the ceria surface in many morphologies and oxidation states—each with differing catalytic properties. In the metallic state, Pd nanoclusters adsorb as a distribution of particle sizes, exposing distinct sites on surface facets, corners, edges, and terraces. On exposure to oxidizing conditions, Pd-based catalysts can form various PdO_x surface and bulk phases, again with a wide distribution of unique surface sites.[18−20] Pd can incorporate itself in the ceria lattice, forming $Pd_xCe_{1-x}O_\delta$ mixed oxides with catalytic properties that vary greatly from supported PdO_x clusters.[21] Since each surface morphology offers distinct catalytic properties, optimizing Pd/CeO_2 catalysts requires a detailed understanding of the structure of the catalyst surface as a function of varying reaction conditions and preparation methods. As such, we combine stability analysis derived from the formalism of ab initio thermodynamics with kinetic arguments to better

Received: April 9, 2015
Revised: September 5, 2015
Published: September 14, 2015

DOI: 10.1021/acscatal.5b00741
ACS Catal. 2015, 5, 6187−6199

understand how the stability of various Pd/CeO_2 surface morphologies affects the overall catalytic activity.

Numerous studies have highlighted the importance of the interaction between Pd and the ceria support, suggesting that the Pd−ceria interfacial region offers unique catalytic properties.[5,9,17,22−30] Cargnello et al.[6] have reported the synthesis of core−shell style catalysts, in which a Pd cluster is encapsulated by a ceria shell ($Pd@CeO_2$), that demonstrate high methane combustion rates below 400 °C. Using kinetic data taken between 220 and 270 °C, the authors demonstrate that the activation barrier over $Pd@CeO_2$ catalysts is similar in magnitude to barriers over traditional Pd−ceria catalysts with metallic clusters adsorbed on the ceria surface. This suggests that the same low-temperature activation site involving a synergistic interaction between Pd and CeO_2 is present on both catalysts. In $Pd@CeO_2$ catalysts, nearly the entire Pd cluster surface is in contact with the ceria lattice, maximizing the number of active sites in comparison to traditional Pd−ceria catalysts, where such sites are only exposed on the contact line at the metal cluster−oxide support boundary. Colussi et al.[5,14] reported catalysts featuring highly active $Pd_xCe_{1-x}O_\delta$ mixed oxides prepared with a solution combustion synthesis (SCS) technique, which achieved combustion rates significantly faster than those for samples prepared by incipient wetness impregnation (IWI). Combined HRTEM and DFT analyses identified stable Pd^{2+} surface states in the SCS samples with Pd atoms incorporated in the $CeO_2(110)$ surface at vacant Ce lattice positions. Such sites were absent in the IWI samples, leading to the conclusion that the incorporated Pd^{2+} states play a key role in increasing catalytic activity toward methane oxidation.

The exceptional activity of ceria-supported Pd catalysts in comparison to other supports points to an activation mechanism that is fundamentally different from the mechanism over palladium oxide. Activation on PdO_x, which is the widely regarded active phase of palladium for hydrocarbon oxidation, has been extensively investigated both experimentally and computationally.[31−34] These studies demonstrate that the methane activation barrier is lowest on the PdO(101) surface, over which CH_4 forms a precursor σ complex when it is adsorbed over exposed Pd atoms that are coordinatively unsaturated (cus-Pd).[33−38] In the precursor state, electrons from C−H bonding orbitals are donated to available 4d states in the exposed metal atom, inducing a back-donation of charge from the metal into the antibonding molecular orbitals of CH_4 in the precursor state. This in turn leads to a low 0 K C−H activation barrier (0.65 eV relative to the adsorbed precursor state, 0.50 eV relative to gas-phase CH_4), as the C−H bonds are destabilized. Over the PdO(100) surface, the methane activation barrier (1.22 eV) is 0.55 eV higher because all exposed Pd atoms reside in saturated square-planar oxygen coordinations that do not allow Pd to strongly interact with methane.[32,33] Since Pd−ceria interactions clearly enhance catalytic activity, ceria must either modulate the σ-complex activation route or offer a fundamentally different route with activity similar to or higher than that of the PdO(101) surface. Experimentally identified structures of $Pd_xCe_{1-x}O_\delta$ clearly indicate that Pd^{2+} exists on the surface in a square-planar coordination environment analogous to the PdO(100) surface,[5,39] suggesting that the σ-complex activation route may not be responsible for the high activity of catalysts containing $Pd_xCe_{1-x}O_\delta$ surface structures.

Previously, our group has demonstrated that Pd atoms incorporated in the $CeO_2(111)$ surface may undergo a facile $Pd^{4+} \rightarrow Pd^{2+}$ transition upon methane activation, leading to a combustion rate many orders of magnitude faster than that for Pd or PdO surfaces.[9−11] A subsequent ab initio thermodynamics investigation suggested that the Pd^{4+} state of a single incorporated Pd atom can be stable under extremely oxidizing conditions; however, this study could not definitively determine if the Pd^{4+} state could exist under typical low-temperature combustion conditions.[12] Indeed, Boronin et al.[39] reported XPS and XRD results identifying stable Pd^{2+} states in $Pd_xCe_{1-x}O_\delta$, in agreement with the surface structure reported by Colussi et al.[5] Despite this evidence demonstrating the stability of the Pd^{2+} surface state, neither investigation conducted structure characterizations under reaction conditions and, therefore, cannot evaluate the possibility that transient Pd^{4+} states play a role in the activation mechanism.

Although the above studies underscore the importance of strong Pd−ceria interactions, the structure and nature of the active site under reaction conditions is still not well understood. In this work, we use DFT and ab initio thermodynamics to examine methane activation over $Pd_xCe_{1-x}O_\delta$ surface models featuring varying Pd oxidation states. We show that the Pd^{2+} surface state is thermodynamically more stable under relevant reaction conditions; nevertheless, a lower apparent barrier is achieved if oxidation of the Pd^{2+} state to a Pd^{4+} state precedes C−H bond activation. Hence, transient Pd^{4+} states play an important role in methane activation over Pd-doped ceria, as incorporation in the ceria lattice enables $Pd^{4+} \leftrightarrow Pd^{2+}$ transitions at the active site, yielding rapid catalytic turnover.

2. THEORY AND METHODS

2.1. DFT Calculations. *2.1.1. Electronic Structure Calculations.* DFT calculations were completed with the Vienna ab initio simulation package (VASP).[40,41] Exchange-correlation energy was calculated with the generalized gradient approximation (GGA), implemented in the Perdew−Wang formulation (PW91).[42] An energy cutoff threshold of 450 eV was employed to truncate plane-wave basis sets. Core electronic regions were represented by the projector augmented wave pseudopotential approximation[43] (PAW), with electronic valence configurations of $5s^25p^66s^24f^15d^1$ for Ce atoms, $4d^{10}$ for Pd atoms, $2s^22p^4$ for O atoms, $2s^22p^2$ for C atoms, and $1s^1$ for H atoms. All calculations were treated as spin polarized, and when appropriate, multiple spin states were tested to ensure that the optimal spin state was identified. Monkhorst−Pack[44] (MP) Brillouin zone sampling was used with a $2 \times 2 \times 1$ MP k-point spacing, where a 15 Å vacuum layer separated images perpendicular to the surface. Molecule calculations were conducted in a 15 Å × 15 Å × 15 Å periodic cell at the Γ point. We employed the Hubbard + U correction[45,46] to treat the well-documented deficiency of standard DFT when describing localized Ce 4f states that may become occupied during surface reduction processes, such as hydrogen adsorption or oxygen vacancy formation.[11,47,48] We used a correction value of U = 5 eV on Ce 4f states, which was determined by previous studies to yield proper electronic occupations in localized Ce 4f states.[49−52] It is possible that a similar deficiency may affect the occupation and energy of partially localized Pd 4d states, which has been less widely investigated in the literature. All values reported in the main text of this work were obtained without applying the +U correction to Pd states; however, we have assessed the relative

DOI: 10.1021/acscatal.5b00741
ACS Catal. 2015, 5, 6187−6199

effect differing U values (applied to the 4d states of Pd) have on the results and conclusions obtained herein, which is discussed in the Supporting Information. Optimized structures were determined by conjugant gradient structural relaxations employed with an atomic force convergence criterion of 0.05 eV $Å^{-1}$. Coordinates of optimized surface structures and total DFT energies are provided in the Supporting Information.

2.1.2. $Pd_xCe_{1-x}O_\delta$ Surface Models. We investigate methane activation over ceria (111) and (110) surfaces with Pd atoms substitutionally incorporated in fluorite ceria at Ce lattice positions. The $CeO_2(111)$ surface was modeled with a periodic 13.32 Å × 11.36 Å orthogonal unit cell consisting of three O−Ce−O trilayers in the z direction perpendicular to the surface, totaling 36 Ce atoms and 72 O atoms in the stoichiometric $CeO_2(111)$ surface, as shown in Figure 1. During structural

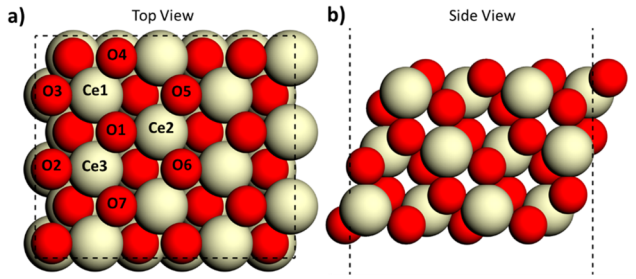

Figure 1. (a) Top and (b) side views of the orthogonal $CeO_2(111)$ unit cell. The $Pd_xCe_{1-x}O_\delta(111)$ surface was built by replacing atoms Ce1−Ce3 with Pd atoms and removing atoms O1−O3.

optimizations, atoms in the bottommost O−Ce−O trilayer were constrained to their bulk lattice positions, while the remaining two surface trilayers were permitted to relax. To test convergence with respect to slab thickness, calculations were also performed on surface models containing four O−Ce−O trilayers, again with atoms in the bottom trilayer constrained to bulk positions. The three-layer model results in surface formation energies for the $Pd_3Ce_{33}O_{69}(111)$ and $Pd_3Ce_{33}O_{70}(111)$ surfaces that are converged to within 0.01 eV of the energies obtained with the four-layer model, indicating that the three-layer model yields sufficiently converged energetics for this study.

The $Pd_xCe_{36-x}O_{72-y}(111)$ surface models (where x equals 1−3 and y is the number of oxygen vacancies) were constructed by directly substituting Ce surface atoms (labeled Ce1−Ce3 in Figure 1) with Pd atoms. Oxygen vacancy formation was treated by successively removing surface oxygen atoms adjacent to incorporated Pd atoms (labeled O1−O7 in Figure 1). Forces on atoms were then reminimized, allowing for local restructuring of the ceria surface after each Pd substitution or oxygen vacancy formation. Multiple initial local configurations were considered as needed to enhance the likelihood of identifying a global minimum energy structure, with the lowest energy and corresponding structure reported. Vacancy formation energies were calculated for each of the labeled oxygen vacancy sites, where only the energy of the preferred vacancy site is reported. This was repeated for surfaces with multiple oxygen vacancies, where the optimized singly vacant surface served as the starting point for identifying the second oxygen vacancy site, continuing until the number of oxygen vacancies exceeded the number of incorporated Pd atoms by 1. The $CeO_2(110)$ surface was modeled with a periodic 10.86 Å × 7.68 Å orthogonal unit cell consisting of five O−Ce−O trilayers in the z direction perpendicular to the surface, totaling 20 Ce atoms and 40 O atoms in the stoichiometric $CeO_2(110)$ surface. Varying oxidation states of the $Pd_2Ce_{18}O_{40-y}(110)$ surface were treated by adding O atoms to the $Pd_2Ce_{18}O_{38}(110)$ surface structure shown in Figure 2, which

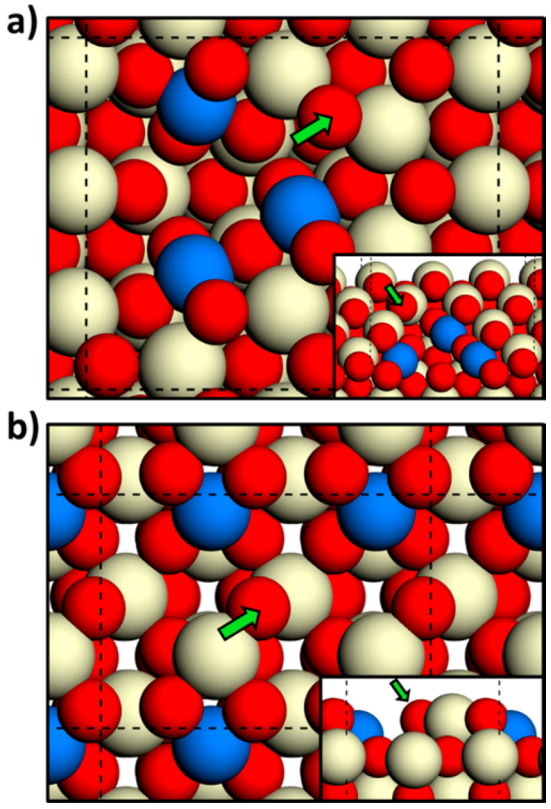

Figure 2. (a) Optimized (111)-$3Pd^{2+}$ surface and (b) (110)-$2Pd^{2+}$ surface. The insets give side views of each surface. The unit cell is indicated by black dashed lines, and the green arrows indicate the favored hydrogen adsorption site during methane activation.

already contains two oxygen vacancies (y = 2). The structure in Figure 2 was previously identified by Colussi et al.[5] with HRTEM experiments, making it a more suitable starting point for modeling varying O vacancy concentrations than the stoichiometric $Pd_2Ce_{18}O_{40}(110)$ surface.

2.2. Ab Initio Thermodynamics. We employ the formalism of ab initio thermodynamics[53] to assess the relative stability of varying $Pd^{\delta+}$ incorporated states and Pd^0 adsorbed states as a function of oxygen pressure and temperature. Following the methodology described in previous work,[12] we define the free energy of a Pd/CeO_2 surface relative to fully oxidized PdO_2 and CeO_2 systems. The free energy of Pd-incorporated and Pd-adsorbed surface states are determined by the following formulas, respectively:

$$G_{\text{surf}}^{\text{Pd-inc}} = E_{N_{\text{Pd-surf}}} + N_{\text{Pd}}E_{\text{CeO}_2} + N_{\text{O-vac}}\frac{1}{2}\mu_{\text{O}_2} - \left(E_{\text{CeO}_2\text{-surf}} + N_{\text{Pd}}\left\{E_{\text{PdO}} + \frac{1}{2}\mu_{\text{O}_2}\right\}\right) \quad (1)$$

$$G_{\text{surf}}^{\text{Pd-ads}} = E_{N_{\text{Pd-surf}}} + N_{\text{Pd}}\frac{1}{2}\mu_{\text{O}_2} - (E_{\text{CeO}_2\text{-surf}} + N_{\text{Pd}}E_{\text{PdO}}) \quad (2)$$

DOI: 10.1021/acscatal.5b00741
ACS Catal. 2015, 5, 6187−6199

Scheme 1. Total Apparent Barrier for CH_4 Activation over the Thermodynamically Favored Pd^{n+} State in Comparison to an Oxidized $Pd^{(n+m)+}$ State, Where the $Pd^{(n+m)+}$ State Yields (a) Lower and (b) Higher Apparent Barriers Depending on the Stability of the $Pd^{(n+m)+}$ State[a]

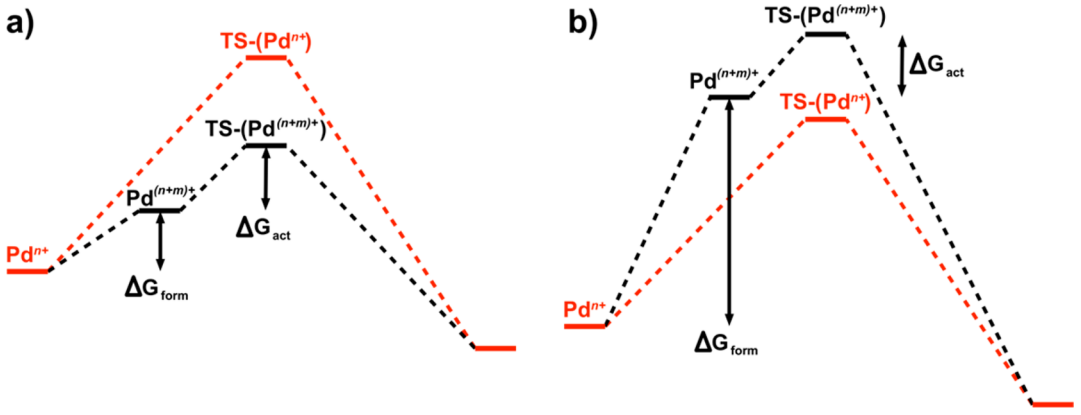

[a]That is, depending on the magnitude of ΔG_{form}.

where $G_{surf}^{Pd\text{-}inc}$ is the free energy of a Pd-incorporated surface and $G_{surf}^{Pd\text{-}ads}$ is the free energy of a Pd-adsorbed surface. N_{Pd} is the number of Pd atoms in the unit cell, $N_{O\text{-}vac}$ is the number of surface oxygen vacancies relative to the stoichiometric CeO_2 surface, $E_{N_{Pd\text{-}surf}}$ is the DFT energy of the Pd-incorporated or Pd-adsorbed surface, E_{CeO_2} and E_{PdO} are the energies of the CeO_2 and PdO bulk references (calculated per stoichiometric formula unit), and $E_{CeO_2\text{-}surf}$ is the energy of the clean CeO_2 surface. Here we neglect entropy and enthalpy corrections to free energy for bulk and surface structures, as these corrections are negligible.[53] Finally, μ_{O_2} is the chemical potential of the O_2 reference calculated using statistical mechanical arguments for gas-phase molecules:

$$\mu_{moleule} = E_{DFT} + E_{ZPV} + H_{thermal} - (S_{trans} + S_{vib} + S_{rot} + S_{elec})T \quad (3)$$

where E_{DFT} is the electronic ground state energy, E_{ZPV} is zero-point vibrational energy, $H_{thermal}$ is the thermal enthalpy correction, and the S terms are translational, vibrational, rotational, and electronic entropy contributions to the total free energy. Calculated values of each term in eq 3 are provided in Table S1 of the Supporting Information. Using the above formulas, we can predict the relative thermodynamic stability of surfaces with varying Pd-dopant morphologies, oxygen vacancy concentrations, and surface oxidation states. Thus, the dominant surface state under operating conditions can be identified as a function of oxygen pressure and temperature.

2.3. Calculation of Apparent Combustion Rates. We calculate and compare apparent methane activation rates over possible Pd−ceria surface morphologies to identify the favored catalytic surface for methane activation. As shown previously,[9,54] the catalytic combustion of methane on Pd−ceria proceeds through a rate-limiting C−H activation step as methane dissociatively adsorbs on the catalyst surface as H* and CH_3* through hydrogen abstraction. Furthermore, the activation barrier for dissociative adsorption can be approximated by calculating the energy of a pseudobarrier structure consisting of an adsorbed H* atom and a gas-phase $^{\bullet}CH_3$ radical above the surface.[9,10] Hence, the pseudobarrier approximation for methane activation is calculated with the formula

$$\Delta G_{act} = E_{surf\text{-}H} + E_{ZPV\text{-}H} + \mu_{^{\bullet}CH_3} - (E_{surf\text{-}clean} + \mu_{CH_4}) \quad (4)$$

where $E_{surf\text{-}H}$ is the energy of the H-adsorbed surface, $E_{ZPV\text{-}H}$ is the zero-point vibrational energy of the H-adsorbed surface, $E_{surf\text{-}clean}$ is the energy of the clean surface, μ_{CH_4} is the chemical potential of CH_4 in the gas phase, and $\mu_{^{\bullet}CH_3}$ is the chemical potential of the $^{\bullet}CH_3$ radical in the pseudotransition state. Chemical potentials of CH_4 and $^{\bullet}CH_3$ were calculated as a function of partial pressure and temperature using eq 3. Translational and rotational contributions in eq 3 were set to 0 for $^{\bullet}CH_3$ in the pseudotransition state, as the $^{\bullet}CH_3$ radical has no translational or rotational degrees of freedom in the activated complex over the oxide surface. All pseudobarriers were calculated with CH_4 and $^{\bullet}CH_3$ molecules treated in simulation cells separate from the oxide surface, unless specifically noted. Additionally, we conducted climbing image nudged elastic band (CI-NEB)[55,56] calculations to identify the true transition state in select cases to validate the pseudobarrier approach. The magnitude of error introduced by the pseudobarrier approach does not alter any conclusions and will be further addressed in section 3.

2.3.1. Apparent Barrier. The thermodynamic stability analysis presented in section 3.2 can be combined with the above barrier calculations to derive an expression for the apparent activation barrier over Pd-incorporated sites in varying oxidation states. Although a particular oxidation state may not be thermodynamically favored, it may offer a lower apparent activation barrier despite forming through an endergonic oxidation step prior to C−H activation. This is demonstrated by the following elementary steps in which a Pd^{n+} incorporated atom is oxidized by gas-phase O_2 prior to the dissociative adsorption of methane:

$$\text{A:} \quad [{*}Pd^{n+}] + \frac{m}{2}O_2 \rightleftharpoons [{*}Pd^{(n+2m)+}] \quad (5)$$

$$\text{B (RDS):} \quad [{*}Pd^{(n+2m)+}] + CH_4 \rightarrow [{*}(CH_3 + H)] \quad (6)$$

where $[{*}Pd^{n+}]$ represents a site adjacent to an incorporated Pd atom in the thermodynamically favored n+ oxidation state and $[{*}Pd^{(n+2m)+}]$ represents the site in an $(n+2m)$+ oxidation state after m oxygen atoms have adsorbed on the surface. The free

DOI: 10.1021/acscatal.5b00741
ACS Catal. 2015, 5, 6187−6199

energy change in step A is obtained from the free energy of each state calculated by eq 1:

$$\Delta G_{\text{form}} = G_{\text{Pd}^{(n+2m)+}} - G_{\text{Pd}^{n+}} = E_{\text{Pd}^{(n+2m)+}} - \left(E_{\text{Pd}^{n+}} + \frac{m}{2}\mu_{\text{O}_2}\right) + \Delta E_{\text{ZPV}} \quad (7)$$

This free energy is related to the equilibrium constant, K_A, of step A and is then combined with the rate constant of activation step B, k_B, to yield the rate expressions

$$K_{\text{A}} = \exp\left(\frac{-\Delta G_{\text{form}}}{RT}\right) = \frac{[*\text{Pd}^{(n+2m)+}]}{[*\text{Pd}^{n+}]P_{\text{O}_2}^{m/2}} \quad (8)$$

$$k_{\text{B}} = \frac{kT}{h}\exp\left(\frac{-\Delta G_{\text{act}}}{RT}\right) \quad (9)$$

$$r = k_{\text{B}}[*\text{Pd}^{(n+2m)+}]P_{\text{CH}_4} = K_{\text{A}}k_{\text{B}}[*\text{Pd}^{n+}]P_{\text{O}_2}^{m/2}P_{\text{CH}_4} \quad (10)$$

The apparent barrier for activation over incorporated Pd in a particular oxidation state thus consists of the activation barrier summed with the free energy difference in comparison to the most stable oxidation state:

$$k_{\text{app}} = K_{\text{A}}k_{\text{B}} = \frac{kT}{h}\exp\left(\frac{-(\Delta G_{\text{act}} + \Delta G_{\text{form}})}{RT}\right) \quad (11)$$

$$\Delta G_{\text{app}} = \Delta G_{\text{act}} + \Delta G_{\text{form}} \quad (12)$$

where k is the Boltzmann constant, h is the Planck constant, ΔG_{form} is the endergonic free energy difference between the n+ and $(n+2m)$+ states obtained from eq 7, and ΔG_{act} is the activation barrier obtained from eq 4. Since ΔG_{form} depends on μ_{O_2}, the apparent barrier is a function of oxygen pressure, in addition to temperature and methane pressure. This formalism, summarized in Scheme 1, captures the balance between site activity and stability required to compare the apparent activity of Pd-incorporated sites in varying oxidation states. This allows us to identify less stable oxidation states that are highly reactive and are stable enough to appear as transient active sites, as depicted in Scheme 1.

3. RESULTS

3.1. Surface Oxidation States. To identify appropriate models of Pd-incorporated surface states, we assess the effects of oxygen vacancy formation on the oxidation state and local geometry of incorporated Pd atoms in the CeO_2 lattice. As reported by Mayernick et al.,[11] direct substitution of a single Pd atom in the stoichiometric CeO_2 surface without oxygen vacancies yields a Pd^{4+} oxidation state, and the formation of an oxygen vacancy results in a $Pd^{4+} \rightarrow Pd^{2+}$ reduction. In the 4+ state, Pd takes an octahedral oxygen coordination characteristic of a d^6 metal center and in the 2+ state takes a square-planar coordination characteristic of a d^8 metal center. Here we investigate the oxidation behavior and geometry of CeO_2 surface models containing multiple Pd atoms, which better approximate the interfacial region between a partially embedded Pd cluster and the ceria surface. Again, direct Pd substitution results in octahedral Pd^{4+} states for all surface Pd atoms. Sequential oxygen vacancy formations result in the reduction of adjacent Pd atoms until all Pd atoms are in a square-planar coordination with a 2+ oxidation state. This is demonstrated in Figure 2 showing square-planar Pd^{2+} states in the optimized surface structures of both the $Pd_3Ce_{33}O_{69}(111)$ and $Pd_2Ce_{18}O_{38}(110)$ surfaces, where the number of oxygen vacancies in each model equals the number of incorporated Pd atoms. The Pd−O bond lengths in the square-planar units range from 1.98 to 2.05 Å, comparable to bond distances of 2.06 Å in bulk PdO.[20] Further oxygen removal results in $Ce^{4+} \rightarrow Ce^{3+}$ reductions of two surface Ce atoms adjacent to the oxygen vacancy, as opposed to further reduction of Pd atoms. This was confirmed by Bader[57,58] charge differences and DOS imaging showing charge accumulation on Ce atoms adjacent to oxygen vacancy sites, which is provided in Table S2 and Figure S7 of the Supporting Information.

Since the oxidation state of incorporated Pd atoms is determined by the amount of oxygen present in the surface model, we will refer to Pd and Ce oxidation states to indicate the amount of oxygen in each surface model. Hence, the $Pd_3Ce_{33}O_\delta(111)$ surface containing zero, one, two, three, or four oxygen vacancies will be respectively referred to as the (111)-$3Pd^{4+}$, (111)-$1Pd^{2+}$/$2Pd^{4+}$, (111)-$2Pd^{2+}$/$1Pd^{4+}$, (111)-$3Pd^{2+}$, and (111)-$3Pd^{2+}$/$2Ce^{3+}$ surfaces. The same naming convention will be used for all surface models.

3.2. Apparent Activation Barriers. Apparent activation barriers were calculated over the $Pd_xCe_{1-x}O_\delta$ (111) and (110) surface models at varying oxidation states using the coupled ab initio thermodynamics/pseudobarrier approach described above. We calculated the barrier for activation occurring over every surface oxygen atom in each model and report here the lowest barrier obtained for each oxidation state. The favored activation sites on the (111)-$3Pd^{2+}$ and (110)-$2Pd^{2+}$ surfaces reside atop oxygen atoms adjacent to two Ce surface atoms that are in turn adjacent to the Pd^{2+} square-planar formation, as indicated in Figure 2 by green arrows. The activation site was similar on the remaining surface models, which are provided in Figures S2 and S3 of the Supporting Information. Attempts to adsorb hydrogen directly on the Pd metal center were unsuccessful, as H migrated to an adjacent oxygen atom in all cases. Furthermore, attempts to locate precursor CH_4 adsorbed states indicated weak interaction between CH_4 and Pd metal centers, with typical exothermic CH_4 adsorption energies less than 0.04 eV relevant to a gas-phase CH_4 molecule in a separate simulation cell. The lack of a bound CH_4 precursor indicates that methane does not form an activated σ complex over $Pd_xCe_{1-x}O_\delta$ surfaces, as it does over cus-Pd atoms on the PdO(101) surface.

The apparent methane activation barrier was determined for each surface oxidation state either by CI-NEB or by using the pseudobarrier approximation, shown in eq 4, with H adsorbed on the surface at the optimal site. A CI-NEB transition state search was completed over the (111)-$1Pd^{4+}$/$2Pd^{2+}$ surface, shown in Figure 3, where the CI-NEB search consisted of four equally spaced images between the initial CH_4 state and the (H^* + $^\bullet CH_3$) pseudotransition state. The CI-NEB transition state (Figure 3b) has forces converged to within 0.05 eV/Å and was validated by a single imaginary vibrational mode along the reaction coordinate. As seen in the figure, the CI-NEB barrier is 0.04 eV higher in energy than the pseudobarrier, demonstrating reasonable accuracy in the pseudobarrier approximation. An equivalent CI-NEB transition state search conducted over the (111)-$3Pd^{2+}$ surface did not yield a converged transition state structure and indicated a monotonic rise in the potential energy surface from CH_4 to (H^* + $^\bullet CH_3$). The resulting barriers for each surface oxidation state are reported in Table 1, along with

DOI: 10.1021/acscatal.5b00741
ACS Catal. 2015, 5, 6187−6199

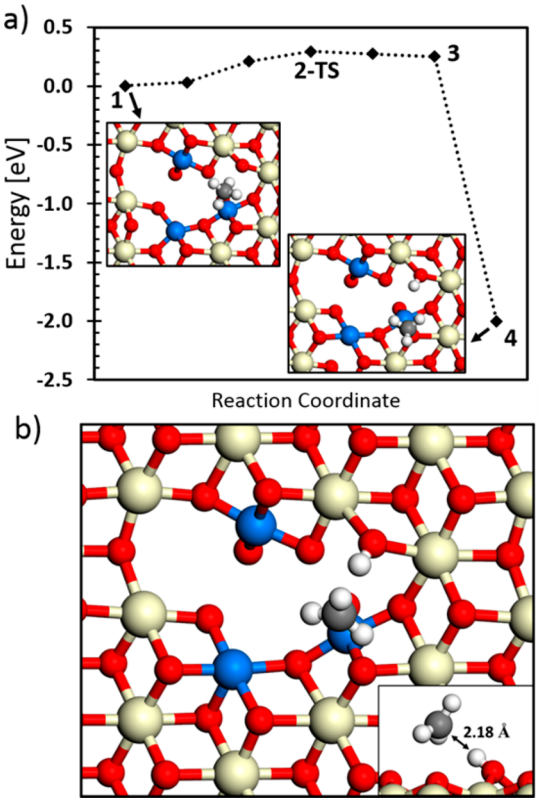

Figure 3. (a) Reaction energy diagram for methane activation over the (111)-1Pd^{4+}/2Pd^{2+} surface, where the data points represent (1) the initial CH_4 state, (2) the transition state identified with CI-NEB, (3) the pseudotransition state consisting of H* and $^{\bullet}CH_3$ away from the surface, and (4) the final CH_3* + H* state. Points between 1 and 3 were obtained by CI-NEB with four equally spaced images between the initial state 1 and the pseudotransition state 3. (b) Structure of the transition state corresponding to the 2-TS labeled point in the reaction energy diagram.

barriers reported in the literature for activation over various CeO_2, PdO, and Pd surfaces.

The 0 K barrier over surfaces containing Pd^{4+} states are 0.29, 0.38, and 0.42 eV over the (111)-1Pd^{4+}/2Pd^{2+}, (111)-2Pd^{4+}/1Pd^{2+}, and (111)-3Pd^{4+} surfaces, respectively. These are significantly lower than the 0.68 eV barrier over the (111)-3Pd^{2+} surface, demonstrating the high activity of the Pd^{4+} state. A similar result was obtained for (110)-2Pd^{2+} and (110)-1Pd^{4+}/1Pd^{2+} surfaces, with 0 K barriers of 1.29 and 0.05 eV, respectively. The Pd^{4+} state serves as a reduction center facilitating hydrogen abstraction during methane activation. Hence, the additional oxygen atom, coupled with the associated Pd^{4+} center, is highly reactive and can readily activate C−H bonds through hydrogen abstraction.

The additional adsorbed oxygen atom is reactive because it is unstable, which must be accounted for when calculating the total apparent barrier. This is demonstrated in Figure 4, which

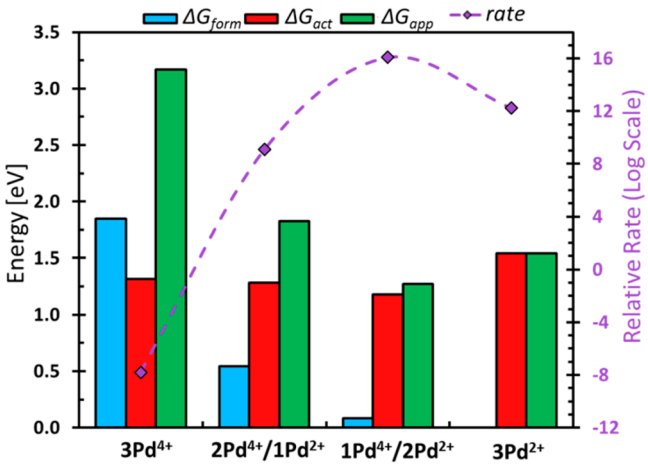

Figure 4. Formation energy (blue), activation energy (red), and total barrier (green) for methane activation over the $Pd_xCe_{1-x}O_\delta(111)$ surface at varying Pd oxidation states under catalytic combustion conditions (T = 400 K, P_{O_2} = 0.01 atm, and P_{CH_4} = 0.01 atm). Purple data points correspond to relative methane activation rates normalized against the rate over clean $CeO_2(111)$.

compares the formation energy, activation energy, total apparent barrier, and relative reaction rate for each oxidation state of the $Pd_3Ce_{33}O_\delta(111)$ surface. The data in the figure are

Table 1. Activation Barriers, Formation Energies, Total Apparent Barriers, and Relative Reaction Rates for Methane Activation over Pd, PdO, CeO_2, and Pd/CeO_2 Surfaces[a]

surface	ΔG_{act}(0 K)	ΔG_{act}(400 K)[b]	ΔG_{form}(400 K)[b]	ΔG_{total}(400 K)[b]	rel rate
$CeO_2(111)$[9]	1.65	2.55[c]		2.55	1 (normalized)
Pd*/$CeO_2(111)$[9]	1.30	2.20[c]		2.20	2.6×10^4
Pd(111)[32]	0.86	1.76[c]		1.76	9.0×10^9
Pd(100)[32]	0.73	1.63[c]		1.63	3.6×10^{11}
PdO(100)[32]	1.22	2.12[c]		2.12	2.6×10^5
PdO(101)[32]	0.50	1.40[c]		1.40	2.8×10^{14}
O-PdO(101)	0.04[e]	0.94	0.61	1.55	3.7×10^{12}
(111)-3Pd^{4+}	0.42[d]	1.32	1.85	3.17	1.6×10^{-8}
(111)-2Pd^{4+}/1Pd^{2+}	0.38[d]	1.28	0.55	1.83	1.2×10^9
(111)-1Pd^{4+}/2Pd^{2+}	0.29[e]	1.19	0.08	1.27	1.2×10^{16}
(111)-3Pd^{2+}	0.68[d]	1.58		1.58	1.7×10^{12}
(110)-2Pd^{4+}	0.01[d]	0.91	2.94	3.85	3.8×10^{-17}
(110)-1Pd^{4+}/1Pd^{2+}	0.05[d]	0.95	0.91	1.86	4.0×10^8
(110)-2Pd^{2+}	1.29[d]	2.19		2.19	3.2×10^4

[a]Barriers are calculated relative to gas-phase CH_4. [b]Conditions: T = 400 K, P_{CH_4} = 0.01 atm, P_{O_2} = 0.01 atm. [c]Applied $T\Delta S$ = 0.9 eV correction to 0 K barrier. [d]Calculated with the pseudobarrier approximation. [e]Calculated with CI-NEB.

DOI: 10.1021/acscatal.5b00741
ACS Catal. 2015, 5, 6187−6199

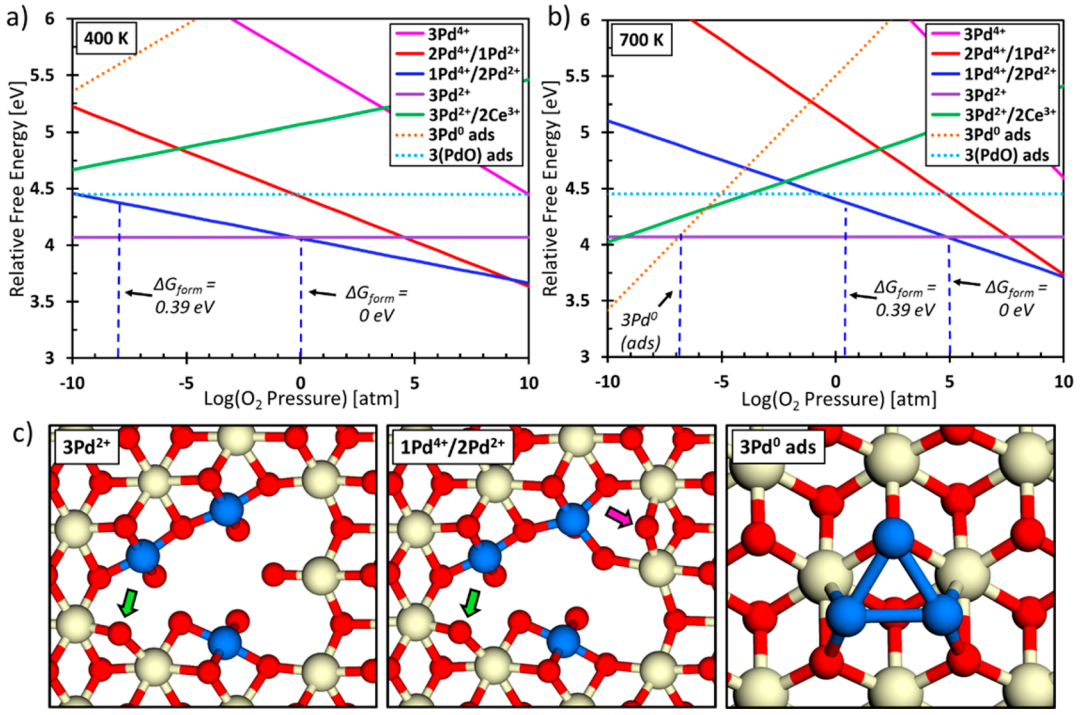

Figure 5. Relative free energy of $Pd_3Ce_{33}O_\delta(111)$ surfaces with varying Pd oxidation states at (a) 400 K and (b) 700 K. The vertical dashed blue lines indicate the pressure region in which the free energy differences between the (111)-$3Pd^{2+}$ and the (111)-$1Pd^{4+}/2Pd^{2+}$ surfaces are 0 eV (where the two surface phases are in equilibrium) and 0.39 eV (where the surfaces have the same apparent methane activation barrier). (c) Structures of the three surfaces that can be thermodynamically stable under the shown (*T*,*P*) ranges. Green arrows indicate the favored hydrogen adsorption site during methane activation, and the magenta arrow indicates the additional adsorbed oxygen atom in the (111)-$1Pd^{4+}/2Pd^{2+}$ surface in comparison to the (111)-$3Pd^{2+}$ surface.

calculated at T = 400 K, P_{O_2} = 0.01 atm, and P_{CH_4} = 0.01 atm, which are representative of the low-temperature onset of the methane oxidation light-off curve during catalytic combustion.[6] At T = 400 K and P_{O_2} = 0.01 atm, the (111)-$3Pd^{2+}$ state is thermodynamically favored and hence has a ΔG_{form} value of 0—in agreement with experimental HRTEM, XPS, and XRD[5,39] observations of the Pd^{2+} state in Pd/Ce mixed oxides. However, the optimal methane activation rate is achieved over the (111)-$1Pd^{4+}/2Pd^{2+}$ state, despite the additional energy required to oxidize the thermodynamically stable (111)-$3Pd^{2+}$ state. This result demonstrates a trade-off between site stability and activity typical in heterogeneous catalysis, where unique catalytic activity can occur near phase boundaries over metastable surface states. Although the (111)-$1Pd^{4+}/2Pd^{2+}$ state is less stable than the (111)-$3Pd^{2+}$ state, the uphill free energy "penalty" required to obtain the Pd^{4+} state (ΔG_{form}) does not outweigh the decrease in ΔG_{act} obtained by forming the Pd^{4+} state (i.e., the situation depicted in Scheme 1a). Comparatively, the free energy penalty required to obtain multiple Pd^{4+} states far outweighs the barrier reduction achieved by the (111)-$2Pd^{4+}/1Pd^{2+}$ and (111)-$3Pd^{4+}$ surfaces, resulting in slower apparent activation rates (as depicted in Scheme 1b). Hence, the Pd^{4+} state is active in temperature and pressure ranges where the magnitude of ΔG_{form} is smaller than the difference in ΔG_{act} between the Pd^{2+} and Pd^{4+} states. This result is generalized over all temperature and oxygen pressure ranges in section 3.3.

3.3. Temperature and Pressure Ranges of Stability and Activity. The calculated free energies and apparent barriers presented in section 3.2 can be generalized to extract boundaries in (*T*,*P*) space demarcating where each oxidation state is thermodynamically stable or kinetically active. This is demonstrated in Figure 5a,b, where the free energy of each oxidation state of the $Pd_3Ce_{33}O_\delta(111)$ surface is plotted against oxygen pressure at 400 and 700 K, respectively. At 400 K, the (111)-$3Pd^{2+}$ state is thermodynamically stable (i.e., has the lowest free energy) at oxygen pressures below 1 atm, above which the (111)-$1Pd^{4+}/2Pd^{2+}$ state is stable. At 700 K, the boundary separating the (111)-$3Pd^{2+}$ and (111)-$1Pd^{4+}/2Pd^{2+}$ states shifts to 10^5 atm, and the adsorbed $3Pd^0$ cluster becomes stable at 10^{-7} atm—in agreement with the expectation that Pd is more easily reduced at higher temperatures. We additionally investigated the stability of an adsorbed $(PdO)_3$ cluster, which was modeled by adsorbing three oxygen atoms at high-symmetry sites of the supported Pd_3 cluster model. As seen in Figure 5a,b, the supported $(PdO)_3$ cluster is less stable than the (111)-$3Pd^{2+}$ surface at all pressures and temperatures, demonstrating that oxidized Pd-incorporated states are more stable than small $(PdO)_x$ clusters supported on the surface.

The vertical dashes in Figure 5 represent the pressure range at each temperature where the (111)-$1Pd^{4+}/2Pd^{2+}$ state has the lowest apparent barrier despite having a higher free energy than the (111)-$3Pd^{2+}$ state. This region begins when the free energy of the (111)-$3Pd^{2+}$ state is 0.39 eV lower than that of the (111)-$1Pd^{4+}/2Pd^{2+}$ state, at which point the apparent activation barriers over the two states are equal. It then extends to the intersection point where the free energy difference between the states is 0 eV, where the (111)-$1Pd^{4+}/2Pd^{2+}$ state becomes thermodynamically stable. Since the difference in activation energy between the states is independent of temperature and oxygen pressure, the range of free energy difference (0–0.39

DOI: 10.1021/acscatal.5b00741
ACS Catal. 2015, 5, 6187–6199

eV) is the same at both 400 and 700 K but is shifted to higher oxygen pressures at higher temperatures (Figure 5b).

The boundaries identified in Figure 5 are generalized over (*T*,*P*) space in the ab initio phase diagram shown in Figure 6. In the figure, regions with solid color shading separated by solid lines represent ranges of thermodynamic stability for each oxidation state. At low temperatures and high oxygen pressures, it is thermodynamically favorable for oxygen to adsorb on the oxide surface creating Pd^{4+} states. At high temperatures and low oxygen pressures, it is favorable for oxygen to desorb, leaving reduced Pd^{2+} and Ce^{3+} states. The $3Pd^{2+}$ state clearly dominates the room-temperature/low-pressure region, in agreement with HRTEM and XPS investigations identifying stable Pd^{2+}-incorporated surface states.[5,39] The adsorbed $3Pd^{0}$ cluster is stable in the region above the orange dotted line, which reflects the propensity for Pd to migrate from the CeO_2 lattice and sinter into large metal clusters under reducing conditions.[25] At P_{O_2} = 1 atm, the Pd^{0} boundary lies near ~1000 K, similar to the experimentally determined PdO → Pd transition at 1050 K for bulk palladium oxide.[59] Additionally, incorporated Pd states are not thermodynamically stable relative to bulk Pd or bulk PdO under these conditions, which is reflected by the positive formation energies for Pd-incorporated states evident in Figure 5 (calculated relative to bulk PdO). This demonstrates that there is a thermodynamic driving force for Pd to egress from incorporated states and sinter into large Pd or PdO clusters. However, incorporated Pd states are thermodynamically stable relative to small $(PdO)_3$ and Pd_3 clusters under the conditions of interest ($T \approx 400-600$ K and $P_{O_2} \approx 10^{-4}$ to 1 atm). We can therefore expect the kinetics of the sintering processes to be slow because the formation of small Pd clusters, which must precede the formation of large clusters, is not thermodynamically favored under the low-temperature conditions considered in this study.

In Figure 6, the purple-blue striped region represents the temperature and pressure ranges where the (111)-$3Pd^{2+}$ state is

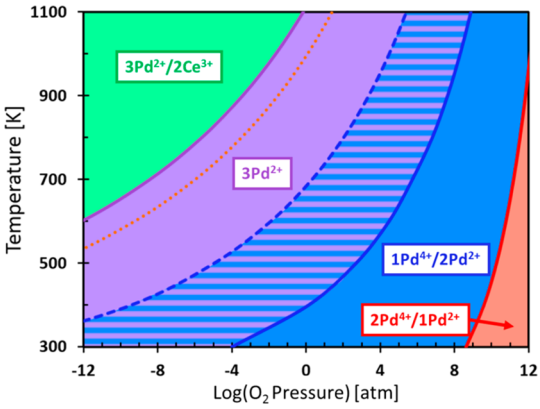

Figure 6. Phase diagram describing Pd oxidation states in the $Pd_3Ce_{33}O_\delta(111)$ surface derived from ab initio thermodynamics. The solid shaded regions separated by solid colored lines indicate thermodynamically stable regions in (*T*,*P*) space. The striped region and dashed line indicate the region where the $3Pd^{2+}$ surface is thermodynamically stable, yet methane activation is kinetically preferred through the $2Pd^{2+}/1Pd^{4+}$ state. An adsorbed $3Pd^{0}$ cluster is thermodynamically stable above the orange dotted line.

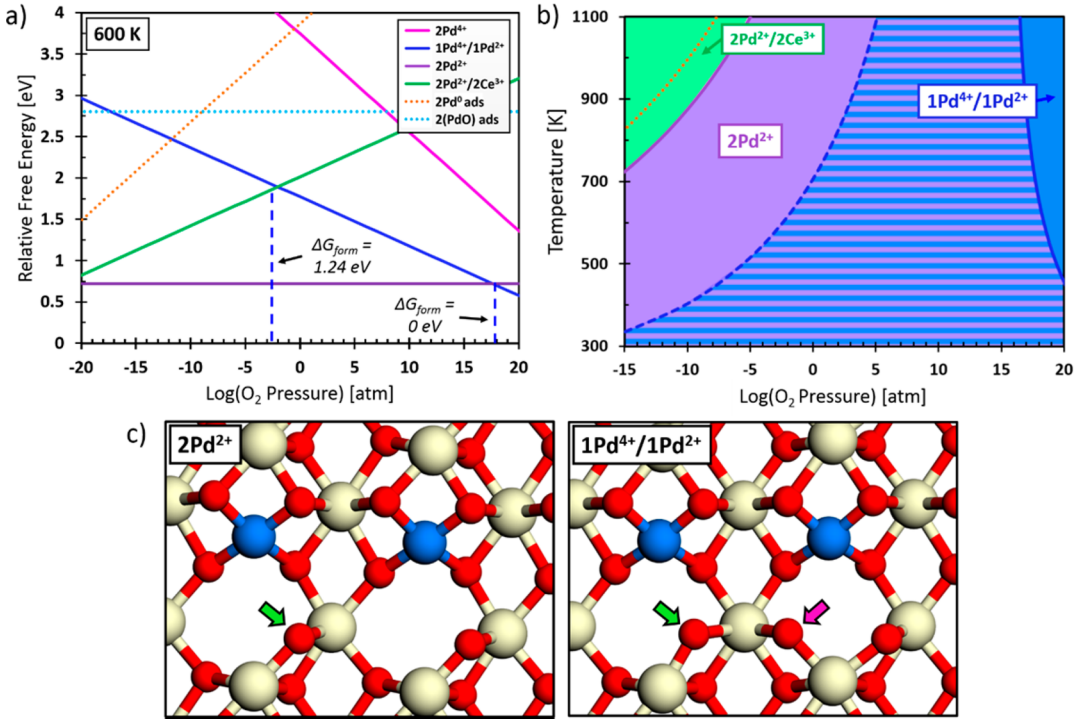

Figure 7. (a) Relative free energy of $Pd_2Ce_{18}O_\delta(110)$ surfaces with varying Pd oxidation states at 600 K. (b) Phase diagram describing oxidation states of Pd in the surface. The striped region and dashed line indicate the region where the $2Pd^{2+}$ surface is thermodynamically stable, yet methane activation is still kinetically preferred through the $1Pd^{2+}/1Pd^{4+}$ site. An adsorbed $2Pd^{0}$ dimer is thermodynamically stable above the orange dotted line. (c) Structure of relevant surfaces under catalytic combustion conditions. Green arrows indicate the favored hydrogen adsorption site during methane activation, and the magenta arrow indicates the additional adsorbed oxygen atom in the (110)-$1Pd^{4+}/1Pd^{2+}$ surface in comparison to the (110)-$2Pd^{2+}$ surface.

DOI: 10.1021/acscatal.5b00741
ACS Catal. 2015, 5, 6187–6199

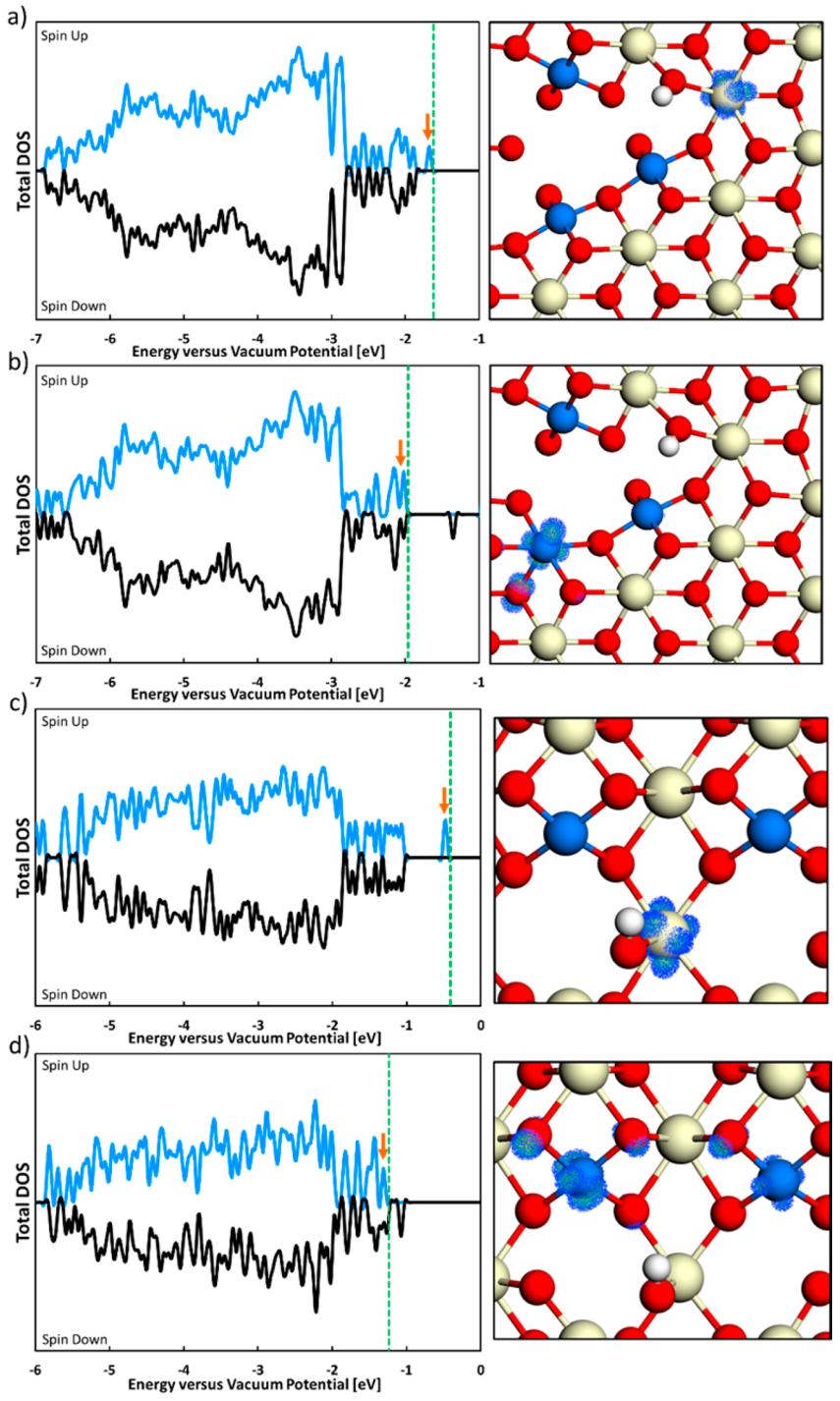

Figure 8. Total DOS (left) and orbital image (right) of the hydrogen abstraction process on (a) the (111)-3Pd^{2+} surface, (b) the (111)-2Pd^{2+}/1Pd^{4+} surface, (c) the (110)-2Pd^{2+} surface, and (d) the (110)-1Pd^{2+}/1Pd^{4+} surface. The Fermi level is indicated by the vertical dashed line, and the orange arrow indicates the state imaged in the right-side panels, where only atoms in the surface layer are shown.

stable, yet the apparent methane activation barrier is lower over the (111)-1Pd^{4+}/2Pd^{2+} state. This unique kinetic region extends over typical operating conditions for low-temperature catalytic combustion, demonstrating that the Pd^{4+} state is likely responsible for the experimentally observed low-temperature activity of $Pd_xCe_{1-x}O_\delta$ catalysts. The same methodology was further applied to the $Pd_xCe_{1-x}O_\delta$(110) surface model, which is summarized in Figure 7. The (110)-2Pd^{2+} state, whose structure is identical with the experimentally determined structure reported by Colussi et al.,[5] is stable over nearly all pressure ranges at low temperatures, in agreement with the HRTEM result identifying the Pd^{2+} incorporated state. The Pd^{4+} state is not stable until unphysically high oxygen pressures are reached, explaining why this state in not observed experimentally under ex situ conditions. Nevertheless, the (110)-1Pd^{4+}/1Pd^{2+} state yields a lower apparent barrier than the (110)-2Pd^{2+} state over the majority of the low-temperature region, indicating again that the Pd^{4+} state provides a unique active site for low-temperature catalytic combustion. Furthermore, the existence of the kinetic region between the Pd^{2+}/Pd^{4+}

DOI: 10.1021/acscatal.5b00741
ACS Catal. 2015, 5, 6187−6199

phase boundaries was also identified for $Pd_xCe_{1-x}O_\delta(111)$ surface models with one and two incorporated atoms (provided in Figure S4 of the Supporting Information), indicating that this result is general to $Pd_xCe_{1-x}O_\delta$ surface phases and is not dependent on the particular choice of surface model.

3.4. Electronic Structure upon Hydrogen Abstraction.

The active nature of the Pd^{4+} state is further demonstrated by analyzing the density of states (DOS) of the $Pd_xCe_{1-x}O_\delta$ surface upon hydrogen abstraction. Figure 8a,b shows the total DOS of the (111)-1Pd^{4+}/2Pd^{2+} and (111)-3Pd^{2+} surfaces with a single hydrogen adsorbed in the pseudotransition state structure, where the vertical green line denotes the Fermi level. Over the (111)-3Pd^{2+} surface, hydrogen adsorption leads to a high-energy isolated spin state characteristic of a $Ce^{4+} \rightarrow Ce^{3+}$ surface reduction. Orbital imaging of this state further confirms that it corresponds to the 4f state of the surface Ce atom adjacent to the hydrogen adsorption site, shown in the right-side panel of the figure. Over the (111)-1Pd^{4+}/2Pd^{2+} surface, hydrogen abstraction reduces a surface Pd atom, which is demonstrated in the figure by the orbital image of the highest energy state below the Fermi level. The highest energy state clearly belongs to a localized Pd 4d state, which resides at a lower energy relative to the vacuum potential reference than the Ce 4f state. The Fermi level of the (111)-1Pd^{4+}/2Pd^{2+} surface is 0.34 eV lower in energy than that of the (111)-3Pd^{2+} surface, which approximately corresponds to the difference in activation energies between the two surface states.

This is further demonstrated over the $Pd_2Ce_{18}O_\delta(110)$ surface in Figure 8c,d. Similar to the case for the $Pd_3Ce_{33}O_\delta(111)$ surface, hydrogen abstraction over the (110)-2Pd^{2+} state induces a high-energy single spin state corresponding to an occupied Ce 4f orbital. This state is clearly absent over the (110)-1Pd^{4+}/1Pd^{2+} surface, where again the highest occupied state corresponds to a Pd 4d state. In this case, the difference in Fermi level between the (110)-1Pd^{4+}/1Pd^{2+} and (110)-2Pd^{2+} states is 0.83 eV. This is again similar in magnitude to the barrier difference between the two oxidation states of this surface, demonstrating that the Pd^{4+} state serves as a favorable reduction center facilitating hydrogen abstraction.

It is clear that additional localized Pd 4d states become occupied after methane activation over Pd^{4+} states. Since DFT does not reliably treat such highly localized states,[33] we investigated how the application of the Hubbard + U correction to Pd 4d states affects the energy of reduced $Pd_xCe_{1-x}O_\delta$ surfaces. We calculated hydrogen and oxygen adsorption energies on the (111)-1Pd^{4+}/2Pd^{2+} and (111)-3Pd^{2+} surface states, respectively, at progressively increasing U values ranging from 0 to 7 eV (summarized in Figure S1 of the Supporting Information). We found that the total apparent barrier for methane activation is not affected by the application of a +U correction to Pd 3d states. Increasing values of U enhance the reducibility of the $Pd_3Ce_{33}O_\delta$ surface. Therefore, the U correction yields less favorable oxygen adsorption energies, thus increasing the values of ΔG_{form} to create the Pd^{4+} state. At the same time, however, increasing U values result in lower values for ΔG_{act} over the Pd^{4+} states (i.e., dissociative methane adsorption occurs more readily). Figure S1 demonstrates that the resulting changes to ΔG_{form} and ΔG_{act} are equal in magnitude and that there is no net change to the apparent activation barrier, ΔG_{app}, as a result of the +U correction to Pd 3d states. This reflects the previously identified[10,11] correlation between oxygen vacancy formation energy and methane activation barrier on ceria surfaces.

4. DISCUSSION

The unique nature of the Pd^{4+} incorporated state in $Pd_xCe_{1-x}O_\delta$ surfaces offers a possible explanation for the observed activity increase in ceria-supported Pd catalysts in comparison to other supports. The results presented here suggest that the activation route at the Pd−ceria interface is unlike the favored activation mechanism over PdO surfaces. Over PdO(101), the activation path proceeds through an adsorbed precursor state where CH_4 forms an activated σ-complex with undercoordinated cus-Pd atoms exposed on the surface.[32] Martin et al.[38] demonstrated that the depletion of cus-Pd 5s states in the PdO(101) surface reduces repulsion from approaching CH_4, inducing a bonding interaction in the precursor σ-complex and a reduced activation barrier. Conversely, on the PdO(100) surface all exposed Pd atoms reside in coordinatively saturated square-planar formations, precluding the formation of the activated precursor state.[32] Here we found that the Pd^{2+}-incorporated surface state was thermodynamically favored under typical operating conditions, in agreement with experimental HRTEM, XPS, and XRD observations.[5,39] The stable Pd^{2+} structures identified over a range of Pd surface concentrations and different $Pd_xCe_{1-x}O_\delta$ surface facets all feature stable square-planar configurations. As seen in Figure 5, further reducing the Pd^{2+} states to form cus-Pd sites (i.e., the (111)-3Pd^{2+}/2Ce^{3+} surface state) does not become thermodynamically favorable until high temperatures are reached—at which point it is more favorable for Pd to egress from the lattice and form adsorbed Pd^0 clusters. Similar to the PdO(100) surface, we did not identify a significant CH_4 interaction with the Pd^{2+}-incorporated surface state of $Pd_xCe_{1-x}O_\delta$, as no coordinatively unsaturated Pd atoms are exposed. Rather, the formation of oversaturated Pd^{4+} states leads to a low-energy activation route, despite requiring an endergonic oxidation step prior to activation.

Methane activation over these sites proceeds through hydrogen abstraction to a surface oxygen atom adjacent to Pd^{4+}, where DOS analysis confirms that the Pd^{4+} state serves as a reduction center. Activation over the thermodynamically preferred Pd^{2+} state results in a significantly higher barrier because a Ce^{4+} surface atom, rather than a Pd^{4+} atom, is reduced, leading to an occupied high-energy 4f state. At 0 K, the CI-NEB barrier over the (111)-1Pd^{4+}/2Pd^{2+} state is 0.29 eV, which is 0.39 eV lower than the pseudobarrier over the (111)-3Pd^2 state and 0.21 eV lower than the barrier over the PdO(101) surface. The resulting apparent rate over the (111)-1Pd^{4+}/2Pd^{2+} site at T = 400 K and P_{O_2} = 0.01 atm is $\sim 10^{16}$ times faster than the rate over the clean $CeO_2(111)$ surface, $\sim 10^7$ times faster than the rate over the Pd(111) surface, and $\sim 10^2$ times faster than the rate over the PdO(101) surface (i.e., the experimentally determined active PdO surface during methane oxidation[32]).

The total 0 K activation barrier over the PdO(101) surface (ΔE_{total} = 0.50 eV) is obtained as the sum of the CH_4 adsorption energy to form the σ-complex precursor state relative to the gas phase (ΔE_{ads} = −0.15 eV) and the intrinsic activation barrier to dissociate methane from the precursor state (ΔE_{act} = 0.65 eV).[32] Weaver, Asthagiri, and co-workers[34,35] demonstrate that inclusion of the van der Waals correction, which addresses the well-established deficiency of standard DFT for modeling dispersion interactions, results in significantly stronger CH_4 adsorption (ΔE_{ads} = −0.42 eV) in agreement with experimental TPD adsorption energies. The

DOI: 10.1021/acscatal.5b00741
ACS Catal. 2015, 5, 6187−6199

addition of dispersion corrections also results in a lower activation energy (ΔE_{act} = 0.58 eV), therefore yielding a significantly lower total activation barrier (ΔE_{total} = 0.16 eV) over cus-Pd sites on PdO(101) in comparison to the uncorrected value. The apparent barrier over the (111)-1Pd^{4+}/2Pd^{2+} surface calculated here does not account for dispersion corrections and is therefore more comparable to the uncorrected ΔE_{total} = 0.50 eV barrier over PdO(101), as it is reasonable to expect that dispersion corrections to the adsorbed precursor state will be similar in magnitude over both surfaces.

To test this assumption, we calculated the CH_4 adsorption energy on the (111)-1Pd^{4+}/2Pd^{2+} surface using the empirical DFT-D2 dispersion correction scheme introduced by Grimme.[60] We found that the initial CH_4 adsorbed state of the CI-NEB calculation (Figure 3) has an adsorption energy of ΔE_{ads} = −0.15 eV relative to gas-phase CH_4. The inclusion of dispersive interactions also lowers the energy of the pseudotransition state structure, yielding a dispersion-corrected total activation barrier of 0.09 eV over the (111)-1Pd^{4+}/2Pd^{2+} state. However, a more sophisticated treatment of dispersion (i.e., with xc functionals that better account for dispersion effects, as opposed to the empirical D2 correction) is required to determine the quantitative effect of dispersion on the apparent barrier. However, the empirical correction employed here suggests that dispersion has a similar effect on all barriers compared in this work, and thus it is assumed that this correction will not significantly affect relative reaction rates and barrier differences used to derive the ab initio phase diagrams in Figures 6 and 7.

We further investigated whether a Pd^{4+} state may play a role in methane activation on the PdO(101) surface by calculating ΔG_{form}, ΔG_{act}, and ΔG_{app} over the PdO(101) surface where an oxygen atom is adsorbed over an exposed cus-Pd surface atom (referred to here as the O-PdO(101) surface). Computational details regarding calculations over the PdO(101) surface are provided in the Supporting Information. We found that, at 400 K and P_{O_2} = 0.01 atm, ΔG_{form} for this surface is 0.61 eV (shown in Figure S5 of the Supporting Information). This indicates that the O-PdO(101) surface is not thermodynamically stable, in agreement with previous theoretical results reported by Rogal et al.[61] for PdO surfaces. The activation barrier, ΔG_{act}, over this surface is 0.04 eV, which was calculated with the CI-NEB as shown in Figure S6 of the Supporting Information. This yields a total apparent barrier for the Pd^{4+} activation route over the O-PdO(101) surface that is higher, albeit similar in magnitude, than activation via the σ-complex precursor state on PdO(101). In comparison to Pd−Ce mixed oxide surfaces, the Pd^{4+} state of the O-PdO(101) surface lacks the stabilizing octahedral oxygen coordination offered by Pd incorporation in the fluorite lattice of CeO_2. Activation through the Pd^{4+} state over PdO(101) is therefore only relevant under very oxidizing conditions, as the ΔG_{form} contribution to the total barrier becomes prohibitively high under reducing conditions.

The pseudobarrier approximation used here may systematically underestimate activation barriers. The CI-NEB results shown in Figure 3 and Figure S6 of the Supporting Information, however, demonstrate that the pseudobarrier approximation is reasonable for the $Pd_xCe_{1-x}O_\delta$ surfaces studied herein, as the pseudobarriers are within 0.04 and 0.02 eV of the NEB barriers for activation over the (111)-1Pd^{4+}/2Pd^{2+} and O-PdO(101) surfaces, respectively. Krcha et al. further evaluated the magnitude of error introduced by the pseudobarrier approach, finding that, on average, pseudobarrier approximations for M-doped ceria underestimated the reaction barrier by less than ∼0.25 eV.[10] NEB calculations, presented herein and by Krcha et al.,[10] demonstrate that methane dissociation over $Pd_xCe_{1-x}O_\delta$ surfaces via hydrogen abstraction features a late transition state that must proceed through the pseudobarrier structure. This ensures that the pseudobarrier approach provides a lower bound for the true barrier and, as such, can be used to rule out high-barrier processes.

It is well-known[62,63] that DFT-GGA overestimates the gas-phase O_2 bond energy, with the PW91 functional yielding an $O_2 \rightarrow 2O$ dissociation energy of 6.17 eV in comparison to the experimental[64] value of 5.15 eV. This leads to a $(1/2)\mu_{O_2}$ value that is as much as ∼0.5 eV too stable, shifting the phase boundaries in Figure 6 to higher oxygen pressures. This error improperly increases ΔG_{form} values required to form the Pd^{4+} state, which in turn increases the total apparent barrier, ΔG_{app}, for activation over Pd^{4+} states. Fortunately, the errors introduced by the pseudobarrier approximation and overestimation of $(1/2)\mu_{O_2}$ are in opposite directions, leading to a canceling of errors. These errors preclude direct comparison with experimental phase boundaries but do not affect the conclusion that the Pd^{4+} is active in temperature and pressure regions where the Pd^{2+} state is thermodynamically favored.

It is possible that water desorption may become rate limiting during methane oxidation at low temperatures or at high H_2O pressures. To assess this possibility, we have evaluated the water desorption free energy over $Pd_3Ce_{33}O_{70}(111)$ at 400 K and P_{H_2O} = 0.01 atm (for direct comparison to the methane activation barrier under these conditions). In this study, the appropriate elementary step for H_2O desorption is

$$[(H^*)1Pd^{4+}/2Pd^{2+}] \rightarrow \frac{1}{2}([1Pd^{4+}/2Pd^{2+}] + [3Pd^{2+}]) + \frac{1}{2}H_2O \quad (13)$$

$$\frac{1}{2}G_{desorption} = \frac{1}{2}(G[1Pd^{4+}/Pd^{2+}] + G[3Pd^{2+}] + \mu_{H_2O}) - G[(H^*)1Pd^{4+}/2Pd^{2+}] \quad (14)$$

where $[(H^*)1Pd^{4+}/2Pd^{2+}]$ represents the (111)-1Pd^{4+}/2Pd^{2+} surface with an adsorbed hydrogen atom and $\Delta G_{desorption}$ represents the free energy of H_2O desorption as an oxygen vacancy is created. The chemical potential of H_2O was computed using eq 3, where the entropic and thermal corrections are provided in Table S1 of the Supporting Information. For this step, we calculate that $\Delta G_{desorption}$ = 0.53 eV, which is significantly lower than the methane activation barrier of 1.27 eV under these conditions (as seen in Table 1). At 600 K, which is the upper limit for catalytic combustion via the Pd^{4+} route, the water desorption energy decreases to 0.28 eV in comparison to a CH_4 apparent activation barrier of 1.98 eV. Additionally, the 0 K desorption energy of water, which can be considered as a reasonable activation barrier for the unimolecular desorption step, is 0.95 eV. This is less than the free energy barrier for methane activation, further suggesting that methane activation is the RDS for combustion over the $Pd_3Ce_{33}O_{70}(111)$ surface under the conditions of interest. This is also in agreement with our previous investigation of the rate-determining step during methane oxidation over $Pd_1Ce_{1-x}O_2$ surfaces, where we found that H_2O desorption was not rate limiting at 300 K until oxygen

DOI: 10.1021/acscatal.5b00741
ACS Catal. 2015, 5, 6187−6199

pressures on the order of ~10^{20} atm were reached.[9] A water desorption barrier of 0.53 eV is nevertheless significant, suggesting that water poisoning may play an important role during methane oxidation over these surfaces at low temperatures or high water pressures.

Additionally, hydroxylation may affect the stability and activity of Pd-incorporated states in the ceria surface. Although not considered here, the effect of ceria hydroxylation on the structure and stability of $Pd_xCe_{1-x}O_\delta$ solid solutions was evaluated previously by Gulyaev et al.[39] The authors of this study employed both experimental (XPS, XRD) and theoretical (DFT) methods to determine the local structure of hydroxylated $Pd_xCe_{1-x}O_\delta$ systems. Their XRD results demonstrate that incorporation of Pd in ceria yields the formation of an oxygen vacancy, which in turn allows Pd to assume a square-planar coordination. Their DFT results show that the stability of the Pd incorporated site is enhanced by the dissociative adsorption of water in the oxygen vacancy (i.e., forming two hydroxyl groups neighboring the Pd incorporation site). This demonstrates that ceria hydroxylation will not preclude the formation of $Pd_xCe_{1-x}O_\delta$ solid solutions. Though such hydroxylation would block the necessary oxygen adsorption step required to form the active Pd^{4+} surface state, the analysis provided in the previous paragraph confirms that water desorption would be unlikely to limit the methane oxidation rate, especially at higher operating temperatures.

The surface models investigated here directly model the $Pd_xCe_{1-x}O_\delta$ mixed oxide surface but may also represent a reasonable approximation of the interfacial region between a Pd cluster and the ceria support. The work of Cargnello et al.[6,22] and Colussi et al.[5,14] demonstrate that Pd−ceria morphologies prepared with varying synthesis techniques yield similar activation barriers but that faster rates are obtained when the degree of Pd−ceria interaction is maximized. We find that Pd incorporation in the ceria lattice leads to a metastable Pd^{4+} state that is highly active, which can account for the increased activity seen in catalyst preparation methods that induce Pd mixing into the ceria lattice. Although the Pd^{4+} state may also offer an activation path over PdO, as evidenced by the low activation barrier over the O-PdO(101) state, the formation energy of the O-PdO(101) state in comparison to that of the (111)-1Pd^{3+}/2Pd^{2+} state (0.61 eV versus 0.08 eV at T = 400 K and P_{O_2} = 0.01 atm) further emphasizes the important role incorporation in the ceria lattice plays in stabilizing the active Pd^{4+} state. As such, we propose that the Pd^{4+} activation route plays an important role at the interfacial region between Pd clusters and the ceria support and is not limited to the idealized $Pd_xCe_{1-x}O_\delta$ surface models investigated here. To further explore this possibility, subsequent investigations will directly model the Pd particle−ceria surface interface.

5. CONCLUSIONS

Identifying dopant metal/host oxide combinations with unique interactions not present in the parent systems is essential for tuning catalytic performance. Here this is demonstrated for $Pd_xCe_{1-x}O_\delta$ catalysts, which offer unique catalytic activity toward the low-temperature oxidation of methane. Pd atoms incorporated in the ceria lattice can take on multiple surface morphologies and oxidation states with varying catalytic properties. To investigate possible activation routes over these surfaces, we utilized DFT calculations to determine apparent methane activation barriers over $Pd_xCe_{1-x}O_\delta$ (111) and (110) surfaces. Both the activity and stability of the active state are taken into account using the formalism of ab initio thermodynamics. Thus, the resulting apparent barriers reported here account for temperature and oxygen pressure variations affecting the stability of active Pd^{4+} surface states. The results demonstrate that Pd^{4+} surface states can offer a lower methane activation barrier than analogous Pd^{2+} states under low-temperature conditions. Furthermore, the activation route over $Pd_xCe_{1-x}O_\delta$ surfaces is fundamentally different from that of the PdO(101) surface, as CH_4 does not form a precursor σ-complex over incorporated Pd^{2+} metal centers in the $Pd_xCe_{1-x}O_\delta$ surface. The tradeoff between state stability and activity was demonstrated in ab initio phase diagrams, where we extracted boundaries indicating the stability and activity of each oxidation state as a function of temperature and oxygen pressure.

The results lend insight into the high activity of Pd/CeO_2 catalysts for low-temperature methane oxidation. In agreement with experimental observations, Pd mixing into the ceria lattice yields high activity attributed to metastable Pd^{4+} states. Incorporation in ceria facilitates $Pd^{4+} \leftrightarrow Pd^{2+}$ transitions, as the fluorite lattice allows Pd atoms to shift between octahedral and square-planar oxygen coordination environments. During low-temperature methane oxidation, incorporated Pd sites can be oxidized by reactant O_2, which in turn serve as reduction centers upon methane activation, yielding rapid catalytic turnover. As this behavior is unique to the mixed nature of the oxide, it exemplifies how the chemical interactions between metal dopants and host oxides may be exploited to optimize catalyst design.

■ ASSOCIATED CONTENT

Supporting Information

The Supporting Information is available free of charge on the ACS Publications website at DOI: 10.1021/acscatal.5b00741.

Calculation results demonstrating the effect of the U correction applied to Pd 4d states, optimized DFT structures of clean and H-adsorbed $Pd_3Ce_{33}O_\delta(111)$ and $Pd_2Ce_{18}O_\delta(110)$ surfaces, ab initio phase diagrams for $Pd_xCe_{36-x}O_\delta(111)$ surfaces (where x = 1−2), free energy diagrams for PdO(101) and O-PdO(101) surfaces, the CI-NEB calculation of the methane activation barrier over the O-PdO(101) surface, computational details for PdO(101) surfaces, tabulated entropic contributions to free energies, Bader charges demonstrating surface Ce^{4+} reduction, structural coordinates of surfaces, and DFT total energies (PDF)

■ AUTHOR INFORMATION

Corresponding Author

*E-mail for M.J.J.: mjanik@engr.psu.edu.

Notes

The authors declare no competing financial interest.

■ ACKNOWLEDGMENTS

This research was supported by funding from the National Science Foundation grant CBET-1032979.

■ REFERENCES

(1) McFarland, E. W.; Metiu, H. *Chem. Rev.* **2013**, *113*, 4391−4427.
(2) Gélin, P.; Primet, M. *Appl. Catal., B* **2002**, *39*, 1−37.

DOI: 10.1021/acscatal.5b00741
ACS Catal. 2015, 5, 6187−6199

(3) Choudhary, T. V.; Banerjee, S.; Choudhary, V. R. *Appl. Catal., A* **2002**, *234*, 1−23.
(4) Ciuparu, D.; Lyubovsky, M. R.; Altman, E.; Pfefferle, L. D.; Datye, A. *Catal. Rev.: Sci. Eng.* **2002**, *44*, 593−649.
(5) Colussi, S.; Gayen, A.; Camellone, M. F.; Boaro, M.; Llorca, J.; Fabris, S.; Trovarelli, A. *Angew. Chem., Int. Ed.* **2009**, *48*, 8481−8484.
(6) Cargnello, M.; Jaén, J. J. D.; Garrido, J. C. H.; Bakhmutsky, K.; Montini, T.; Gámez, J. J. C.; Gorte, R. J.; Fornasiero, P. *Science* **2012**, *337*, 713−717.
(7) Farrauto, R. J. *Science* **2012**, *337*, 659−660.
(8) Zhu, Y.; Zhang, S.; Shan, J.-j.; Nguyen, L.; Zhan, S.; Gu, X.; Tao, F. *ACS Catal.* **2013**, *3*, 2627−2639.
(9) Mayernick, A. D.; Janik, M. J. *J. Catal.* **2011**, *278*, 16−25.
(10) Krcha, M. D.; Mayernick, A. D.; Janik, M. J. *J. Catal.* **2012**, *293*, 103−115.
(11) Mayernick, A. D.; Janik, M. J. *J. Phys. Chem. C* **2008**, *112*, 14955−14964.
(12) Mayernick, A. D.; Janik, M. J. *J. Chem. Phys.* **2009**, *131*, 084701−084712.
(13) Colussi, S.; Trovarelli, A.; Cristiani, C.; Lietti, L.; Groppi, G. *Catal. Today* **2012**, *180*, 124−130.
(14) Colussi, S.; Gayen, A.; Llorca, J.; de Leitenburg, C.; Dolcetti, G.; Trovarelli, A. *Ind. Eng. Chem. Res.* **2012**, *51*, 7510−7517.
(15) Adijanto, L.; Bennett, D. A.; Chen, C.; Yu, A. S.; Cargnello, M.; Fornasiero, P.; Gorte, R. J.; Vohs, J. M. *Nano Lett.* **2013**, *13*, 2252−2257.
(16) Wang, X.; Gorte, R. J. *Catal. Lett.* **2001**, *73*, 15−19.
(17) Meng, L.; Lin, J.-J.; Pu, Z.-Y.; Luo, L.-F.; Jia, A.-P.; Huang, W.-X.; Luo, M.-F.; Lu, J.-Q. *Appl. Catal., B* **2012**, *119*−*120*, 117−122.
(18) Lundgren, E.; Gustafson, J.; Mikkelsen, A.; Andersen, J. N.; Stierle, A.; Dosch, H.; Todorova, M.; Rogal, J.; Reuter, K.; Scheffler, M. *Phys. Rev. Lett.* **2004**, *92*, 046101.
(19) Klikovits, J.; Schmid, M.; Merte, L. R.; Varga, P.; Westerström, R.; Resta, A.; Andersen, J. N.; Gustafson, J.; Mikkelsen, A.; Lundgren, E.; Mittendorfer, F.; Kresse, G. *Phys. Rev. Lett.* **2008**, *101*, 266104.
(20) Senftle, T. P.; Meyer, R. J.; Janik, M. J.; van Duin, A. C. T. *J. Chem. Phys.* **2013**, *139*, 044109−044115.
(21) Priolkar, K. R.; Bera, P.; Sarode, P. R.; Hegde, M. S.; Emura, S.; Kumashiro, R.; Lalla, N. P. *Chem. Mater.* **2002**, *14*, 2120−2128.
(22) Cargnello, M.; Fornasiero, P.; Gorte, R. J. *Catal. Lett.* **2012**, *142*, 1043−1048.
(23) Cargnello, M.; Doan-Nguyen, V. V. T.; Gordon, T. R.; Diaz, R. E.; Stach, E. A.; Gorte, R. J.; Fornasiero, P.; Murray, C. B. *Science* **2013**, *341*, 771−773.
(24) Craciun, R.; Daniell, W.; Knözinger, H. *Appl. Catal., A* **2002**, *230*, 153−168.
(25) Misch, L. M.; Kurzman, J. A.; Derk, A. R.; Kim, Y.-I.; Seshadri, R.; Metiu, H.; McFarland, E. W.; Stucky, G. D. *Chem. Mater.* **2011**, *23*, 5432−5439.
(26) Meng, L.; Jia, A.-P.; Lu, J.-Q.; Luo, L.-F.; Huang, W.-X.; Luo, M.-F. *J. Phys. Chem. C* **2011**, *115*, 19789−19796.
(27) Hinokuma, S.; Fujii, H.; Okamoto, M.; Ikeue, K.; Machida, M. *Chem. Mater.* **2010**, *22*, 6183−6190.
(28) Farmer, J. A.; Campbell, C. T. *Science* **2010**, *329*, 933−936.
(29) Chen, C.; Cao, J.; Cargnello, M.; Fornasiero, P.; Gorte, R. J. *J. Catal.* **2013**, *306*, 109−115.
(30) Yang, Z.; Lu, Z.; Luo, G.; Hermansson, K. *Phys. Lett. A* **2007**, *369*, 132−139.
(31) Zhu, G.; Zemlyanov, D. Yu.; Ribeiro, F. H. *J. Phys. Chem. B* **2005**, *109*, 2331−2337.
(32) Hellman, A.; Resta, A.; Martin, N. M.; Gustafson, J.; Trinchero, A.; Carlsson, P. A.; Balmes, O.; Felici, R.; van Rijn, R.; Frenken, J. W. M.; Andersen, J. N.; Lundgren, E.; Grönbeck, H. *J. Phys. Chem. Lett.* **2012**, *3*, 678−682.
(33) Chin, Y.-H.; Buda, C.; Neurock, M.; Iglesia, E. *J. Am. Chem. Soc.* **2013**, *135*, 15425−15442.
(34) Antony, A.; Hakanoglu, C.; Asthagiri, A.; Weaver, J. F. *J. Chem. Phys.* **2012**, *136*, 054702.
(35) Weaver, J. F.; Hakanoglu, C.; Antony, A.; Asthagiri, A. *Chem. Soc. Rev.* **2014**, *43*, 7536−7547.
(36) Weaver, J. F.; Hakanoglu, C.; Hawkins, J. M.; Asthagiri, A. *J. Chem. Phys.* **2010**, *132*, .
(37) Weaver, J. F.; Hinojosa, J. A., Jr.; Hakanoglu, C.; Antony, A.; Hawkins, J. M.; Asthagiri, A. *Catal. Today* **2011**, *160*, 213−227.
(38) Martin, N. M.; Van den Bossche, M.; Hellman, A.; Grönbeck, H.; Hakanoglu, C.; Gustafson, J.; Blomberg, S.; Johansson, N.; Liu, Z.; Axnanda, S.; Weaver, J. F.; Lundgren, E. *ACS Catal.* **2014**, *4*, 3330−3334.
(39) Gulyaev, R. V.; Kardash, T. Y.; Malykhin, S. E.; Stonkus, O. A.; Ivanova, A. S.; Boronin, A. I. *Phys. Chem. Chem. Phys.* **2014**, *16*, 13523−13539.
(40) Kresse, G.; Furthmuller, J. *Comput. Mater. Sci.* **1996**, *6*, 15−50.
(41) Kresse, G.; Furthmuller, J. *Phys. Rev. B: Condens. Matter Mater. Phys.* **1996**, *54*, 11169−11186.
(42) Perdew, J. P.; Chevary, J. A.; Vosko, S. H.; Jackson, K. A.; Pederson, M. R.; Singh, D. J.; Fiolhais, C. *Phys. Rev. B: Condens. Matter Mater. Phys.* **1992**, *46*, 6671−6687.
(43) Kresse, G.; Joubert, D. *Phys. Rev. B: Condens. Matter Mater. Phys.* **1999**, *59*, 1758−1775.
(44) Monkhorst, H. J.; Pack, J. D. *Phys. Rev. B* **1976**, *13*, 5188−5192.
(45) Herbst, J. F.; Watson, R. E.; Wilkins, J. W. *Phys. Rev. B: Condens. Matter Mater. Phys.* **1978**, *17*, 3089−3098.
(46) Anisimov, V. I.; Gunnarsson, O. *Phys. Rev. B: Condens. Matter Mater. Phys.* **1991**, *43*, 7570−7574.
(47) Fabris, S.; de Gironcoli, S.; Baroni, S.; Vicario, G.; Balducci, G. *Phys. Rev. B: Condens. Matter Mater. Phys.* **2005**, *71*, 041102.
(48) Fabris, S.; de Gironcoli, S.; Baroni, S.; Vicario, G.; Balducci, G. *Phys. Rev. B: Condens. Matter Mater. Phys.* **2005**, *72*, 237102.
(49) Da Silva, J. L. F.; Ganduglia-Pirovano, M. V.; Sauer, J.; Bayer, V.; Kresse, G. *Phys. Rev. B: Condens. Matter Mater. Phys.* **2007**, *75*, 045121−045110.
(50) Nolan, M.; Grigoleit, S.; Sayle, D. C.; Parker, S. C.; Watson, G. W. *Surf. Sci.* **2005**, *576*, 217−229.
(51) Nolan, M.; Parker, S. C.; Watson, G. W. *Surf. Sci.* **2005**, *595*, 223−232.
(52) Yang, Z.; Luo, G.; Lu, Z.; Hermansson, K. *J. Chem. Phys.* **2007**, *127*, 074704−074705.
(53) Reuter, K.; Scheffler, M. *Phys. Rev. B: Condens. Matter Mater. Phys.* **2001**, *65*, 035406.
(54) Knapp, D.; Ziegler, T. *J. Phys. Chem. C* **2008**, *112*, 17311−17318.
(55) Henkelman, G.; Uberuaga, B. P.; Jonsson, H. *J. Chem. Phys.* **2000**, *113*, 9901−9904.
(56) Henkelman, G.; Jonsson, H. *J. Chem. Phys.* **2000**, *113*, 9978−9985.
(57) Bader, R. F. W. *Acc. Chem. Res.* **1985**, *18*, 9−15.
(58) Henkelman, G.; Arnaldsson, A.; Jonsson, H. *Comput. Mater. Sci.* **2006**, *36*, 354−360.
(59) Zhang, H.; Gromek, J.; Fernando, G.; Marcus, H.; Boorse, S. *J. Phase Equilib.* **2002**, *23*, 246−248.
(60) Grimme, S. *J. Comput. Chem.* **2006**, *27*, 1787−1799.
(61) Rogal, J.; Reuter, K.; Scheffler, M. *Phys. Rev. B: Condens. Matter Mater. Phys.* **2004**, *69*, 075421.
(62) Curtiss, L. A.; Raghavachari, K.; Redfern, P. C.; Pople, J. A. *J. Chem. Phys.* **1997**, *106*, 1063−1079.
(63) Hammer, B.; Hansen, L. B.; Nørskov, J. K. *Phys. Rev. B: Condens. Matter Mater. Phys.* **1999**, *59*, 7413−7421.
(64) *Handbook of Chemistry and Physics: A Ready Reference Book of Chemical and Physical Data*, 84th ed.; Lide, D. R., Ed.; CRC Press: New York, 2004; pp 5−16.

DOI: 10.1021/acscatal.5b00741
ACS Catal. 2015, 5, 6187−6199